J. Mech. Phys. Solids 160 (2022) 104787

Contents lists available at ScienceDirect

Journal of the Mechanics and Physics of Solids

journal homepage: www.elsevier.com/locate/jmps

Orientation-dependent superelasticity and fatigue of CuAlMn alloy under in situ micromechanical tensile characterization

Mostafa Karami [a], Kangjie Chu [a], Zeyuan Zhu [a], Zhou Wang [b], Qingping Sun [a,c], Mingxin Huang [b], Xian Chen [a,*]

[a] Mechanical and Aerospace Engineering, Hong Kong University of Science and Technology, Hong Kong
[b] Department of Mechanical Engineering, The University of Hong Kong, Pokfulam Road, Hong Kong
[c] HKUST Shenzhen-Hong Kong Collaborative Innovation Research Institute, Futian, Shenzhen, China

ARTICLE INFO

Keywords:
Micromechanical tensile test
Superelasticity
Nano-cavity
Crystallographic anisotropy

ABSTRACT

The in situ micromechanical tensile tests are conducted to characterize the superelastic behaviors for [223], [1 2 14], [325] and [205] oriented $Cu_{67}Al_{24}Mn_9$ micro-slats. The stress-induced martensitic transformations are captured in all textures corresponding to strong crystallographic anisotropy. We propose a one-dimensional constitutive model considering the directional anisotropy of elastic modulus for cubic symmetry and the crystallographic compatibility of twinned martensite. The modeled mechanical behaviors agree with the micromechanical tensile tests well, which suggests that the formation of compatible twins is the primary deformation mechanism. Particularly in the [205] texture, we observed formation of nano-cavities (< 100 nm) on the lateral surface of the micro-slat. Based on the analysis of compatible martensite twin laminates and fcc slip systems, we theorize that the massive normal elongation and little lateral shear cause the formation, stretching and growth of nano-cavities at nano scales to accommodate the external loads. As a result, the structural and functional fatigue resistance is improved compared to other textures. The experimental and theoretical results in this paper are potentially useful to guide the texture design of Cu-based shape memory alloy for high transformation strain and low functional fatigue.

1. Introduction

Shape memory alloys undergoing reversible phase transformations underlie a large category of functional materials widely exploited for biomedical devices, microelectronic actuators and solid-state caloric refrigerators. In tandem with rapid growth of nano-fabrication technologies, sophisticated devices such as self-expanding implants (Morgan, 2004; Chen et al., 2004; Yoneyama and Miyazaki, 2008; Petrini and Migliavacca, 2011), nano-manipulators (Koledov et al., 2019) and neutral stents (Chen et al., 2016) can be materialized at nano to micron sizes, to treat the fatal vascular diseases. The functional stability and fatigue of the phase-transforming material used in nano/micro-devices play a critical role in applications, but the understanding of the micromechanical behaviors is still limited in this field. Compared to the bulk structures, the intrinsic hardening and strengthening of the miniaturized structures are mainly attributed to strain heterogeneity (Nix and Gao, 1998) and dislocation starvation (Greer and Nix, 2006), which are concluded as *smaller is stronger*. For non-transforming metallic crystals, the kinematics and corresponding size effects were studied and verified extensively by various nanomechanics experiments (Greer et al., 2005; Nix and Gao, 1998; Greer and Nix, 2006) and the continuum models (Gao et al., 1999; Huang et al., 2000; Wei and Hutchinson, 2003). For stress-induced transforming crystals, it

* Corresponding author.
E-mail address: xianchen@ust.hk (X. Chen).

https://doi.org/10.1016/j.jmps.2022.104787
Received 23 September 2021; Received in revised form 21 December 2021; Accepted 6 January 2022
Available online 26 January 2022

is reasonable to speculate that the hardening and strengthening follow a similar size dependency, but the coupling of plasticity and phase transformation makes the mechanisms of deformation more complicated. When the superelastic alloys are used in small scales, a higher actuation load must be applied to those tiny devices to drive the demanded displacement, which undoubtedly compromises the reliability of the functional material during the device deployment.

Among shape memory alloys, the equiatomic Ni–Ti (slightly Ni rich) are the mostly studied material system at submicron to tens of microns length scales by micromechanical compression experiments (Frick et al., 2007, 2008; Norfleet et al., 2009; Hua et al., 2018; Kabirifar et al., 2018; Chu et al., 2019; Hua et al., 2020). Besides the evidently seen hardening effect in the elastic regime of austenite, the critical stress, at which the compression-induced martensitic transformation occurs, is observed to increase with the decreasing micropillar diameter, while the superelastic strain is slightly reduced (Frick et al., 2008), compared to the bulk specimen (Sehitoglu et al., 2001). It was also seen that the mechanism of deformation changes from martensitic transformation driven to plasticity driven as the diameter of micropillar becomes less than 1 μm (Frick et al., 2007). The single crystal NiTi micropillars with sizes from 1 μm-diameter (Frick et al., 2007, 2008) to 4 μm-diameter (Pfetzing-Micklich et al., 2012) exhibits magnificent crystallographic anisotropy. Compared to the [001], [101] and [210] oriented micropillars that are fully reversible, the [111] oriented micropillars exhibit a large permanent strain upon unloading, associated with a much higher flow stress upon loading (Frick et al., 2008; Pfetzing-Micklich et al., 2012). As a rough summary over relevant publications for compression-induced superelasticity of bulk and micropillar NiTi, the critical transformation stress increases from 400–600 MPa to 600–800 MPa, while the superelastic strain reduces from 4%–6% to 2%–3% (Karami and Chen, 2021; Frick et al., 2007, 2008; Norfleet et al., 2009; Hua et al., 2018; Kabirifar et al., 2018; Hua et al., 2020; Sehitoglu et al., 2001). Similar texture dependencies were also captured in Cu-based superelastic micropillars, such as Cu–Al–Mn–Ni (Fornell et al., 2017) and Cu–Al–Mn (Karami et al., 2020b). Besides, in typical Cu-based superelastic alloy, particularly the single crystal Cu–Al–Ni system, San Juan, Schuh and their coworkers conducted massive nanomechanics studies on mechanical damping in micropillars and nanopillars (San Juan et al., 2008, 2009, 2012; Gómez-Cortés et al., 2017; Gómez-Cortés et al., 2019), which exhibit drastically increase of transformation stress upon loading and decrease of the reverse transformation stress upon unloading. It makes the Cu-based superelastic alloy system a profound candidate for micromechanical damper devices.

While the studies of non-transforming material systems under microtension have been widely conducted to reveal the size effect of plasticity in various crystals, the microtension experiments are rarely performed to study the superelastic behaviors of shape memory alloys. Kiener, Minors, Greer, Nix and their coworkers are the pioneers who carried out in situ tensile tests under the electron microscopy on non-transforming micro and nano lamellae of single crystals such as easy-to-slip copper, gold and aluminum (Kiener et al., 2008; Kiener and Minor, 2011; Jennings and Greer, 2011; Kim and Greer, 2009; Oh et al., 2009), and hard-to-slip molybdenum, tungsten, tantalum and niobium (Kim and Greer, 2009; Kim et al., 2010, 2012, 2010). Under scanning electron microscopy, the sudden bursts captured by the stress–strain curves can be directly associated with the formation of slips of the tensile micro-slat. The strain-hardening and dislocation starving mechanisms well explain the size dependencies of the micro/nanomechanics of most non-transforming face-centered and body-centered single crystals. When the deformation involving the formation of both slips and twins, and when the flow stress induces both plastic shear bands and martensitic phase transformation, the crystallographic theory of martensite and the plasticity theory should be considered together. From experimental point of view, it is more challenging to conduct the micromechanical tensile test due to the substantial lateral shear deformation caused by the formation of martensite twinning variants. The alignment and geometric matching between the dog-bone or T-shaped micro-slat and the concave grip are critical, sometimes become the single failure factor of the micromechanical tensile test.

In this paper, we conduct a series of in situ micromechanical tensile tests to study the orientation-dependent superelastic behaviors of $Cu_{67}Al_{24}Mn_9$ shape memory alloy. The crystallographic textures are characterized by electron backscatter diffraction near the edge of the well polished specimen. The T-shaped tensile slat is milled by the focused ion beam with the gauge dimensions of $3 \times 1.5 \times 12.8$ μm^3. In order to avoid asymmetric mechanical loading, we designed a flat shoulder for the tensile grip, which transfers the tensile force via a swelling transition to the gauge region. The true stress–strain behaviors are characterized for [223], [1 2 14], [325] and [205] oriented micro-slats, respectively. The superelasticity and its functional degradation exhibit strong crystallographic anisotropy. The crystal plasticity and superelasticity are studied by a one-dimensional thermoelastic constitutive model (Bhattacharya and Kohn, 1996; Sadjadpour and Bhattacharya, 2007) combined with the kinematic compatibility theory of martensite (Ball and James, 1987; Karami et al., 2020b). The martensitic microstructure and defects are observed during the in situ micromechanical tensile tests, which agree with the theoretical prediction of compatible martensitic twin laminates.

2. Experimental methods

2.1. Materials preparation and crystallographic characterizations

A mixture of high-purity Cu (99.99 wt%), Al (99.999 wt%) and Mn (99.95 wt%) ingots were weighted according to the atomic ratio 67 : 24 : 9, which was sealed in a quartz tube for induction melting. The complete alloying process was conducted in the induction furnace under Argon atmosphere. Followed by casting into a cylindrical copper mold, the melt was solidified in a rod-shape of diameter 5 mm. The rod was homogenized at 800 °C for 3 h under an argon atmosphere, then underwent normalizing process to develop uniformly distributed grain sizes. We cut the rod into thin slices of thickness 1 mm, which were sealed in a vacuum quartz tube, annealed at 900 °C for 1 h and quenched into water to obtain martensite. For electron backscatter diffraction, the sample surface was subsequently chemo-mechanically polished by a colloidal silica polishing suspension to remove deformation layer caused by initial mechanical polishing. The sample surface and the sides were all mechanically polished at room temperature

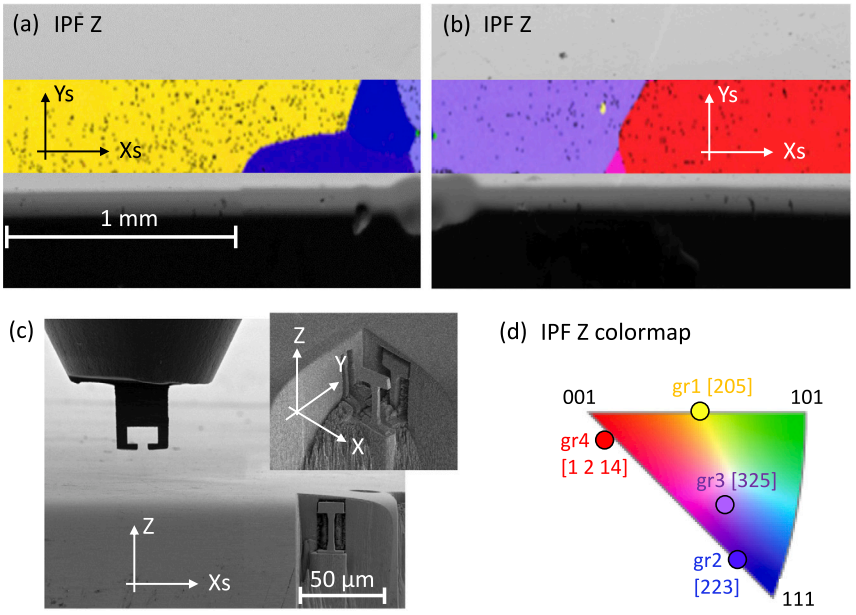

Fig. 1. (a)–(b) The SEM image and corresponding EBSD inverse pole figure (IPF) map obtained from the areas near the edge of bulk sample. (c) The geometric relation between the tensile grip and the sample. (d) IPF Z-axis orientation function.

Table 1
The crystallographic orientations of each of the grains characterized by EBSD in Fig. 1. The components of **X**, **Y** and **Z** are written in cubic basis $\mathbf{e}_1$, $\mathbf{e}_2$ and $\mathbf{e}_3$. The last column lists the nearest rational crystallographic direction to Z axis.

Grain	X	Y	Z	N
gr1 (yellow)	[0.649, −0.721, −0.241]	[0.657, 0.692, −0.299]	[0.224, 0.021, 0.540]	[205]
gr2 (blue)	[−0.872, 0.253, 0.418]	[0.039, −0.817, 0.576]	[0.285, 0.303, 0.411]	[223]
gr3 (purple)	[−0.473, −0.692, 0.545]	[0.736, −0.65, −0.187]	[0.283, 0.183, 0.478]	[325]
gr4 (red)	[0.503, 0.847, −0.173]	[−0.861, 0.508, −0.019]	[0.042, 0.093, 0.576]	[1 2 14]

for structural and crystallographic analysis. The room temperature phase is in face-centered cubic austenite, with lattice parameter $a_0 = 5.87897$ Å (Karami et al., 2020a).

The grain structure and orientations of the polished bulk sample was characterized by electron backscatter diffraction (EBSD) under Zeiss Sigma 300 FEG scanning electron microscope (SEM) with an Oxford Instruments Symmetry detector. We selected two neighboring domains with an area about 4×1.5 mm^2 near the sample edge to conduct the EBSD scans, as shown in Fig. 1(a)–(b) with the stage coordinate system Xs–Ys–Z. Fig. 1(c) shows the geometric relation between the stage and the tensile slat for our in situ micromechanical experiment. The tensile micro-slat is exposed to the e-beam for imaging where the tensile direction is along Z-axis. The transverse and depth directions are denoted as X axis and Y axis. Both counterclockwisely rotate from Xs axis and Ys axis by 45 degree. The EBSD inverse pole figure (IPF) map in Fig. 1(d) reveals four grains with different crystallographic orientations. Let $\mathbf{e}_1$, $\mathbf{e}_2$ and $\mathbf{e}_3$ represent three cubic axes [001], [010] and [001] of austenite. Table 1 gives the components of orthonormal **X** (X axis), **Y** (Y axis) and **Z** (Z axis) vectors written in cubic basis. The Z axis is aligned with the uniaxial loading direction, to which we selected a rational crystallographic direction **N** to represent each of the grains. Note that all calculations related to the tensile direction use the vector **Z** listed in Table 1.

2.2. Fabrication of micro-slat and tensile grip

The free-standing micro-slat was prepared by using FEI Helios G4 UX dual-beam focused ion beam (FIB) milling system. Considering possible finite rotation and twist during the martensitic transformation during loading, we modified the conventional designs (Kiener et al., 2008; Kim and Greer, 2009) of the “shoulder” shape for micro-slat. Instead of an angular shoulder with about 30° inclination from the horizontal direction, we use the focused ion beam to sculpt a T-shaped micro-slat, which can be gripped through a flat shoulder by the tensile grip. Near the corners of the T-shape, we designed a swelling transition from the effective stretching domain to reduce the stress concentration. The final height/width ratio is about 4 with a lath thickness of 1.5 μm and width of 3 μm, shown in Fig. 2. This design allows for a better load balance from both sides and prevent the artificial displacement responses due to bending and twisting. In fact, similar T-shaped gripping designs have been used for nanolamellae in metallic glass (Tian et al., 2012) and diamond (Dang et al., 2021) under in situ nano-tensile test. Both experiments reported unusual

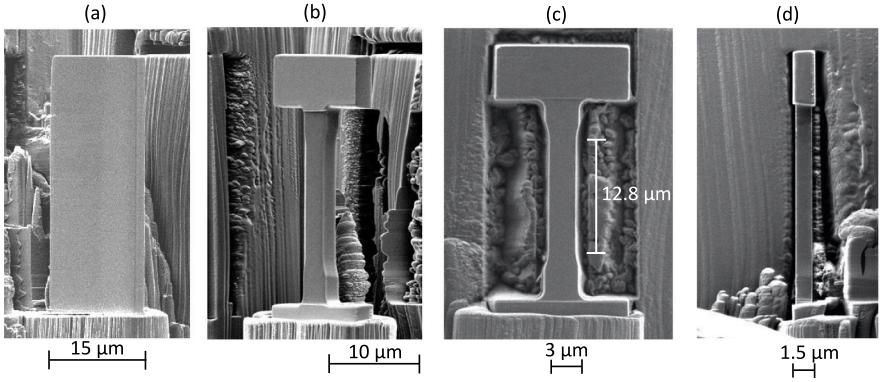

Fig. 2. The SEM images of (a) miniaturized plate as the base for (b)–(d) the T-shaped micro-slat visualized from different angles.

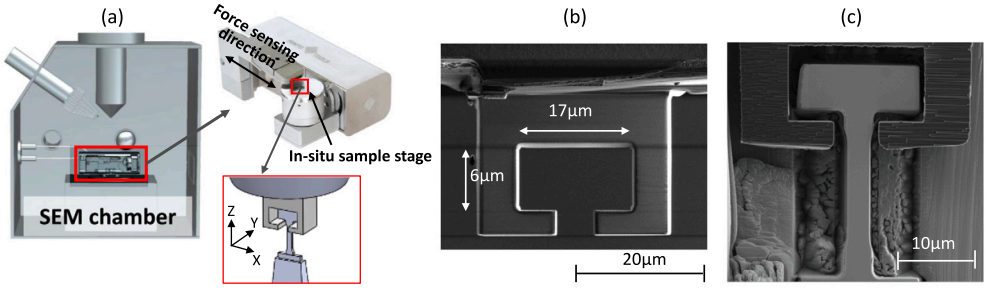

Fig. 3. (a) Schematic illustration of micromechanical tensile setup in SEM chamber, and (b)–(c) SEM images of the tensile grip, and a proper alignment between the micro-slat and the grip.

elastic behaviors in naturally brittle materials. Inspired by their results, we believe that the delicate displacement responses during martensitic phase transformation accompanied with crystal plasticity would be accurately captured by our modified design.

The FIB milling steps for making the micro-slat are concluded as followings. First, a plate with width of 15 μm and thickness of slightly bigger than 3 μm was milled near the edge of the well-polished bulk sample. Its vertical and horizontal tapering were removed by a series low-current milling through the stage rotation and tilting, as indicated in Fig. 2(a). The plate was the base for the micro-slat. Using our self-designed pattern, we milled a T-shape out of the plate, as shown in Fig. 2(b) in two steps with sequentially reduced ion currents. Finally, the lateral surface was machined by low ion currents to remove the damaged layers, finishing with the effective gauge length of 12.8 μm, width of 3 μm and thickness of 1.5 μm, shown in Fig. 2(c)–(d). We used a 20 μm-diameter diamond tip as a precursor to fabricate the tension grip. The geometry is designed to be an inverse to the T-shape. First, we used a high ion current to mill a plate of about 10 μm thickness with small tapering sides, which was machined all through using a designed concave pattern as shown in Fig. 3(b). The T-shaped micro-slat is well fitted in the tensile grip, in Fig. 3(c).

2.3. In situ micromechanical tensile experiment

The in situ uniaxial tensile tests were performed on the T-shaped micro-slats by FemtoTools Nanomechanical Testing System (model FTNMT03, Buchs ZH, Switzerland) under FEI Quanta 250 FEG SEM. Fig. 3(a) shows the experimental configuration how the sample is mounted to the loading cell, and how the loading cell is placed into the SEM chamber. The loading direction is aligned with the Z axis, while the e-beam is parallel to the Y axis for imaging. First, we conducted a nanoindentation test on the surface to calibrate the system compliance, which was used in the analysis of force–displacement data to remove any artificial deformations caused by the grip and loading system. Then the tensile grip is lowered to grasp the tensile micro-slat with proper alignment adjustments. We begun with the tensile test with an increasing maximum load from 1500 μN to 4300 μN at relatively fast loading rate until the superelastic plateau was captured. For $\mathbf{N} = [223]$ orientation, the maximum load was chosen to be 4300 μN, while for $\mathbf{N} = [205], [325], [1\ 2\ 14]$ orientations, the maximum load was selected as 2150 μN. We collected the displacement–force data by the displacement control at a fixed rate of 30 nm/sec to acquire a quasi-static mechanical response for the tensile micro-slat. At pre-stretch, maximum stretch and post-stretch stages, the loading condition is held on for SEM imaging. The formation of microstructure on the lateral side of the micro-slat can be observed and cooperated to the mechanical test. For each of the orientations in Table 1, we performed the cyclic fatigue tests under displacement control at a loading frequency of 0.5 Hz. To minimize the effect of the thermal drift during the long-term cycling experiment, we paused the test and re-calibrated the thermal drift every one hundred cycles. It enables sufficient consistency of the functional degradation and residual strain accumulation over thousands of tensile cycles.

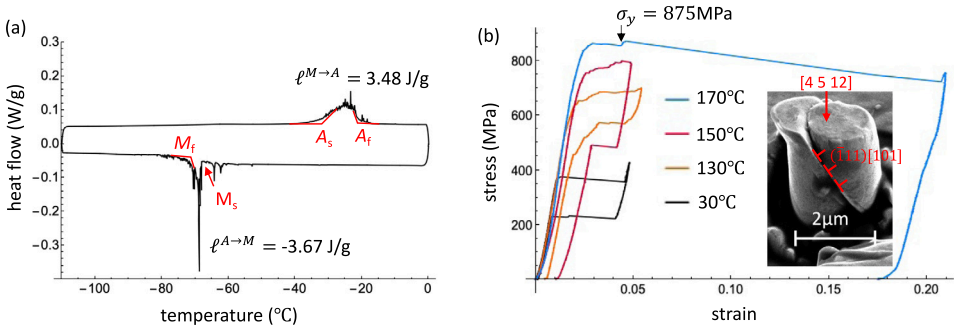

Fig. 4. (a) The DSC analysis of bulk $Cu_{67}Al_{24}Mn_9$ alloy during a thermally driven phase transformation. The onsets on the heating/cooling pathways are denoted as the austenite start/finish and martensite start/finish temperatures, corresponding to the labeled latent heat $\ell^{M\to A}$ and $\ell^{A\to M}$. (b) The true stress–strain curves of the microcompression tests on a 2μm-diameter pillar with orientation [4 5 12] from 30 °C to 200 °C, with an inset of the post-mortem SEM image after unloading at 170 °C.

2.4. Thermoelastic characterization

We used the differential scanning calorimetry (TA Instruments DSC250) to characterize the transformation temperatures and latent heat of the bulk $Cu_{67}Al_{24}Mn_9$ during a full phase transformation from martensite to austenite, then back to martensite. The DSC system was firstly isothermal at −110 °C, then ramped up to 0 °C, finally cooled down to −110 °C at the rate of 10 °C/min.

Considering the stress-induced phase transformations of Cu-based shape memory alloys, the transformation driving force is usually much lower than their yielding limits (San Juan et al., 2009; Fornell et al., 2017; Ni et al., 2016), so is the $Cu_{67}Al_{24}Mn_9$ alloy. From the thermal analysis, the thermally driven transformation of bulk $Cu_{67}Al_{24}Mn_9$ alloy occurs below zero degree Celsius. At room temperature, the stress-induced martensitic transformation happens before yielding. By Clausius–Clapeyron relation, as the testing temperature is elevated, the transformation stress increases. In order to suppress the stress-induced martensitic transformation, and purely drive the slip-only deformation of the miniaturized samples, we sequentially increase the testing temperatures until the yielding happens before the martensitic transformation. We conducted a series of microcompression tests on a 2μm-diameter pillar with orientation [4 5 12] by Hysitron Triboindenter TI 900 from 30 °C to 170 °C. The stress-induced martensitic transformation is observed under 30 °C, 130 °C, 150 °C, with an increasing transformation stress. At 170 °C, the pillar yields before stress-induced phase transformation. Experimentally, this ex situ experiment provides us with important information to retrieve the critical resolved shear stress for the testing material.

3. Results and discussion

3.1. Transformation temperatures, critical resolved shear stress and elastic modulus

From the DSC curve, in Fig. 4(a), we obtained the austenite start/finish temperatures $A_s = -25$ °C, $A_f = 0$ °C, and the martensite start/finish temperatures $M_s = -50$ °C, $M_f = -69$ °C. The amount of latent heat absorbed during heating is $\ell^{M\to A} = 3.48$ J/g from martensite to austenite, while the latent heat emitted during cooling is $\ell^{A\to M} = -3.67$ J/g from austenite and martensite.

From the microcompression results performed under a sequence of increasing temperatures, it is seen that the 2μm-diameter pillar exhibits superelasticity upon loading, and is completely recoverable at 30 °C. In Fig. 4(b), we observed stress-induced martensitic phase transformations corresponding to the superelastic plateaux as the temperature continuous increasing, while prominent residual strain is initially captured at 130 °C. It implies that the yielding and martensitic transformation coexist during the mechanical loading above 130 °C. At 170 °C, the superelastic behavior completely disappears. Thus the pillar yields due to plasticity at temperature 170 °C and beyond with a yielding stress $\sigma_y = 875$ MPa. This corresponds to the surface step observed in the micrograph inset of Fig. 4(b). With respect to the compression direction $\mathbf{c} = -[4\ 5\ 12]$, the maximum Schmid factor is calculated as $m^* = (\mathbf{c}\cdot\mathbf{n})(\mathbf{c}\cdot\mathbf{s})/(|\mathbf{c}|^2|\mathbf{n}||\mathbf{s}|) = 0.459$ for $\mathbf{n} = (\bar{1}11)$, $\mathbf{s} = [101]$ among 12 slip systems of face-centered cubic. The step caused by $(\bar{1}11)[101]$ slip is observed in the post-mortem SEM image in Fig. 4(b), which agrees well with the angle 57° between the slip plane $(\bar{1}11)$ and compression direction [4 5 12]. This experiment characterizes the critical resolved shear stress for the single crystal $Cu_{67}Al_{24}Mn_9$,

$$\tau_{\mathrm{CRSS}} = \sigma_y m^* = 401.6 \text{ MPa}. \tag{1}$$

This value plays a critical role in the microtension experiment to judge whether plasticity or martensitic transformation dominates the kinematics upon the cyclic micromechanical loading.

In the linear elasticity regime of a cubic crystal, when the uniaxial loading direction $\mathbf{N}$ is aligned with one of the $\langle 100\rangle$ directions, the compliance tensor only depends on three independent parameters as

$$\begin{aligned} &S_{1111} = S_{2222} = S_{3333} \equiv S_{11} \\ &S_{1122} = S_{1133} = S_{2211} = S_{3311} = S_{2233} = S_{3322} \equiv S_{12} \\ &S_{1212} = S_{2121} = S_{1313} = S_{3131} = S_{2323} = S_{3232} \equiv S_{44}. \end{aligned} \tag{2}$$

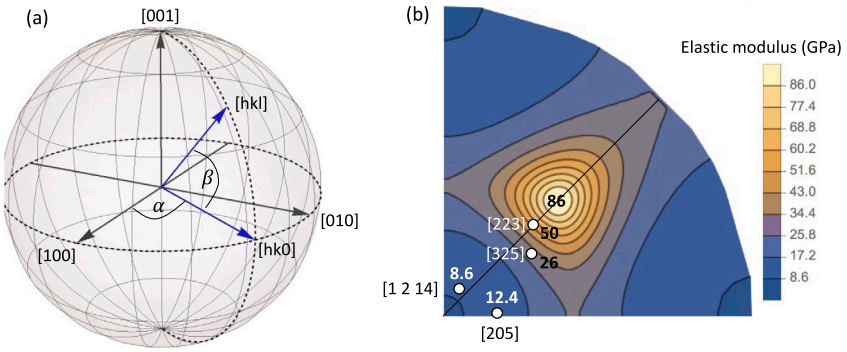

Fig. 5. (a) Angular relations of a crystallographic direction $[hkl]$ with respect to the cubic axes and (b) contours of the directional elastic moduli of the face-centered cubic $Cu_{67}Al_{24}Mn_9$ alloy.

When the uniaxial loading direction $\mathbf{N} = [hkl]$, depicted in Fig. 5(a), that is rotated about [001] axis by angle α from [100], and tilted by angle β from (001) plane, the compliance tensor $\mathcal{S}'$ along the loading direction $[hkl]$ is transformed from the compliance tensor $\mathcal{S}$ along the cubic axis [001] by

$$S'_{ijkl} = Q_{im}Q_{jn}Q_{kp}Q_{lq}S_{mnpq}, \tag{3}$$

where the second order tensor $\mathbf{Q} = \mathbf{Q}_\beta\mathbf{Q}_\alpha \in SO(3)$ for

$$\mathbf{Q}_\alpha = \begin{bmatrix} \cos\alpha & -\sin\alpha & 0 \\ \sin\alpha & \cos\alpha & 0 \\ 0 & 0 & 1 \end{bmatrix}, \quad \mathbf{Q}_\beta = \begin{bmatrix} \cos\beta & 0 & \sin\beta \\ 0 & 1 & 0 \\ -\sin\beta & 0 & \cos\beta \end{bmatrix}. \tag{4}$$

Let the uniaxial stress tensor written as $\boldsymbol{\sigma}_{nn} = \sigma\mathbf{n} \otimes \mathbf{n}$ where σ is the magnitude of the stress corresponding to the unimodular vector $\mathbf{n} \in \mathbb{R}^3$ along the loading direction. The cubic compliance tensor can be determined by uniaxial tensile loading along various linearly independent crystallographic directions. In our experiment, we conducted such an experiment on $Cu_{67}Al_{24}Mn_9$ alloy to measure the magnitude of uniaxial tensile force and the corresponding elongation along four linearly independent crystallographic directions [205], [223], [325] and [1 2 14], by which the elastic modulus can be determined. The orientation dependent elastic modulus is calculated and plotted in Fig. 5(b). Note that the elastic modulus presented here is the directional Young's modulus calculated as $E = 1/S'_{1111}$ by Eq. (3) for a crystallographic direction $[hkl]$. Our uniaxial tensile tests reveal an elastic anisotropy of the $Cu_{67}Al_{24}Mn_9$ alloy with the most stiff direction [111]. The specific values of moduli for each of the tested orientations are given in Section 3.3.

3.2. In situ uniaxial tensile of phase-transforming micro-slat

The uniaxial tensile stress versus strain is presented in Fig. 6(a). We assume that the volume of the micro-slat is conserved during loading. For the measured force F and displacement d, the true stress is calculated as $\sigma = \frac{F}{wt}\frac{\ell+d}{\ell}$ where w, t and ℓ are the width, thickness and length of the effective tensile region of the micro-slat in the reference configuration. The true strain is calculated as $\epsilon = \int_\ell^{\ell+d} \frac{dx}{x} = \ln\frac{\ell+d}{\ell}$. Among four tested orientations, the rigidest orientation is along [223] under the microtension load. The stress-induced martensitic transformations are observed in all tested micro-slats, which are fully reversible upon unloading. Let σ_{cr} be the critical stress under which the martensitic transformation is initially captured upon loading. Both the critical stress σ_{cr} and the transformation strain ϵ_t, *i.e.* the width of strain plateau, exhibit strong crystallographic anisotropy. The [223] oriented micro-slat exhibits the smallest transformation strain under the highest critical stress, while the [1 2 14] and [205] oriented micro-slats show the biggest transformation strain under the lowest critical stress. The [325] oriented micro-slat's superelastic response is moderate compared to other orientations. The microstructure is characterized by SEM in Fig. 6(b)–(e) at pre-transformation (state A - undeformed configuration) and post-transformation (state B - maximum stretched configuration). We observed the leaning twin bands in martensite phase of [223], [325] and [205] textures, which disappear upon unloading. For [1 2 14] oriented micro-slat, it is seen from Fig. 6(a) that about 6% superelastic strain is induced during tensile loading, but the martensitic twin bands were not seen clearly in Fig. 6(c). Besides, formation of nano-cavities is observed on the left edge of the [205] oriented micro-slat. These nano-cavities are almost uniformly distributed in the middle region of the side surface of the micro-slat with diameter of about 100 nm and below. Because the deformation by formation of the martensite is a simple shear with respect to the austenite as the reference configuration, consequently the cavity would appear at either side of the micro-slat, but not at both sides.

To understand the formation of microstructure quantitatively, we analyze the kinematic compatibility of the martensitic phase transformation of the tested alloy by the crystallographic theory of martensite (Ball and James, 1987). It was reported in reference Karami et al. (2020a) that the $CuAl_{24}Mn_9$ undergoes a structural transformation between face-centered cubic ($Fm\bar{3}m$) austenite and orthorhombic ($Pmmn$) martensite. The lattice parameter of cubic phase is $a_0 = 5.87897$ Å, determined by monochromatic X-ray energy scans for specific indexed Bragg peaks. The orthorhombic martensite phase were characterized and analyzed by the derived

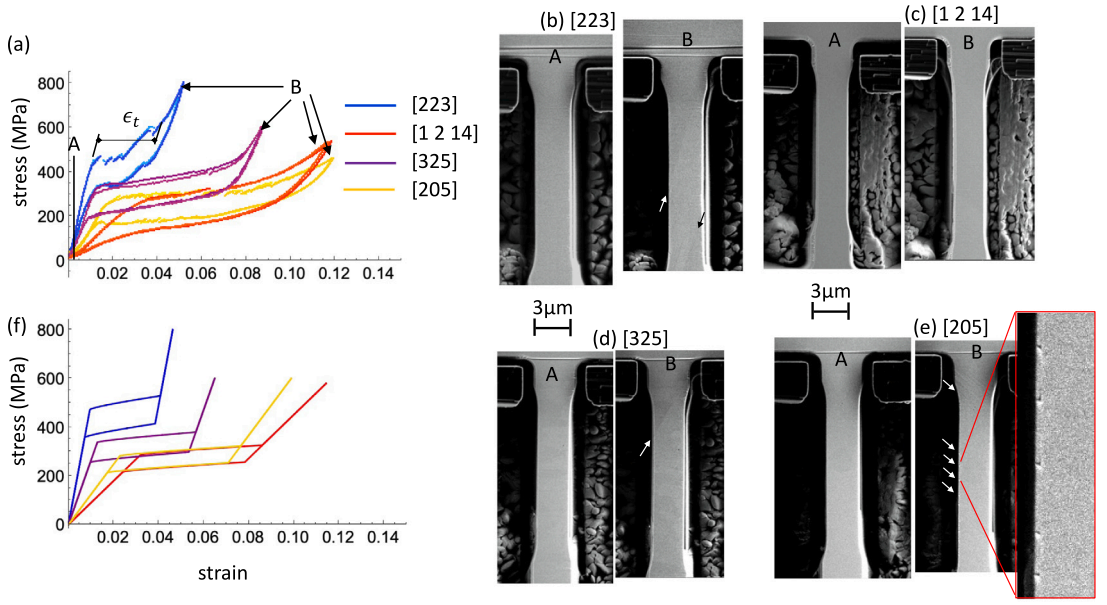

Fig. 6. In situ micromechanical tensile experiments performed for various textures. (a) The true stress–strain curves of the single crystal micro-slat under uniaxial tensile loading along the crystallographic directions [205], [223], [325] and [1 2 14]. The superelastic plateau is labeled by ϵ_t. The insets A and B denote the strain states, at which we collected (b)–(e) SEM images of the lateral side at the undeformed state (A) and the maximum stretched (B) state. The white arrows suggest the martensite microstructure formed in configuration B. The zoomed image of [205] texture shows a sequence of nano-cavities. (f) The stress–strain curves computed by the constitutive model in (14) for the tested orientations.

structure algorithm (Karami et al., 2020a) based on their Laue diffraction patterns and corresponding monochromatic X-ray analysis. The lattice parameters of martensite are refined as $a = 4.43196$ Å, $b = 5.34533$ Å and $c = 4.26307$ Å. On the cubic basis, the transformation stretch tensor is calculated as

$$\mathbf{U} = \begin{bmatrix} \alpha & \beta & 0 \\ \beta & \alpha & 0 \\ 0 & 0 & \gamma \end{bmatrix} \tag{5}$$

where $\alpha = \frac{a+c}{\sqrt{2}a_0}$, $\beta = \frac{-a+c}{\sqrt{2}a_0}$ and $\gamma = \frac{b}{a_0}$. The stretch tensor in Eq. (5) is identified as one of the martensite variants. There are six distinct variants calculated from Eq. (5) by a symmetry-relation $\mathbf{QUQ}^T$ for $\mathbf{Q} \in \mathcal{P}^{24}/\mathcal{P}^4$ where $\mathcal{P}^{24}$ and $\mathcal{P}^4$ denote the point groups of cubic (group order: 24) and orthorhombic (group order: 4). All six martensite variants are expressed as

$$\mathbf{U}_1 = \begin{bmatrix} \alpha & 0 & \beta \\ 0 & \gamma & 0 \\ \beta & 0 & \alpha \end{bmatrix}, \quad \mathbf{U}_2 = \begin{bmatrix} \alpha & 0 & -\beta \\ 0 & \gamma & 0 \\ -\beta & 0 & \alpha \end{bmatrix}, \quad \mathbf{U}_3 = \begin{bmatrix} \gamma & 0 & 0 \\ 0 & \alpha & -\beta \\ 0 & -\beta & \alpha \end{bmatrix}$$
$$\mathbf{U}_4 = \begin{bmatrix} \gamma & 0 & 0 \\ 0 & \alpha & \beta \\ 0 & \beta & \alpha \end{bmatrix}, \quad \mathbf{U}_5 = \begin{bmatrix} \alpha & -\beta & 0 \\ -\beta & \alpha & 0 \\ 0 & 0 & \gamma \end{bmatrix}, \quad \mathbf{U}_6 = \begin{bmatrix} \alpha & \beta & 0 \\ \beta & \alpha & 0 \\ 0 & 0 & \gamma \end{bmatrix}. \tag{6}$$

Three ordered eigenvalues of these symmetry-related variants are

$$(\lambda_1, \lambda_2, \lambda_3) = \left(\frac{b}{a_0}, \frac{\sqrt{2}c}{a_0}, \frac{\sqrt{2}a}{a_0} \right) \text{ with } \lambda_1 < \lambda_2 < \lambda_3. \tag{7}$$

The middle eigenvalue $\lambda_2 = 1.0253$, which implies that the martensite forms as a mixture of fine twins through an elastic transition layer from the austenite due to crystallographic compatibility (Ball and James, 1987). The laminated twin structure, expressed as $(1-f)\mathbf{U}_i | f\hat{\mathbf{R}}_{i,j}\mathbf{U}_j$ for some volume fraction $f \in [0,1]$ and rotation $\hat{\mathbf{R}}_{i,j} \in SO(3)$, satisfies a rank-one relation[1]

$$\hat{\mathbf{R}}_{i,j}\mathbf{U}_j - \mathbf{U}_i = \mathbf{a}_{i,j} \otimes \mathbf{n}_{i,j}, \tag{8}$$

in which $\mathbf{n}_{i,j}, \mathbf{a}_{i,j} \in \mathbb{R}^3$ are the twin plane and twin shear vectors for the pair of variants (i,j). Then, the twin can be expressed by a variant and its twin parameters as $(\mathbf{U}_i, \mathbf{a}_{i,j} \otimes \mathbf{n}_{i,j})$. The interface between the twin laminate in Eq. (8) and austenite is calculated by solving the crystallographic equation

$$\mathbf{R}_{i,j}(\mathbf{U}_i + f\mathbf{a}_{i,j} \otimes \mathbf{n}_{i,j}) - \mathbf{I} = \mathbf{b}_{i,j} \otimes \mathbf{m}_{i,j}, \tag{9}$$

[1] No summation on i, j and so for the calculations beyond.

Table 2
Calculated and measured recoverable strain under uniaxial loading for CuAlMn micro-slats.

N	calculated ϵ_t	measured ϵ_t
[223]	0.0289	0.028
[1 2 14]	0.0499	0.051
[325]	0.0428	0.049
[205]	0.0507	0.058

for the habit plane $\mathbf{m}_{i,j}$ and total shear $\mathbf{b}_{i,j}$ in $\mathbb{R}^3$. The necessary condition that Eq. (9) has a solution for an internally twinned martensite is

$$(\frac{A}{4}+B)B \le 0, \text{ for } A=-2(\mathbf{U}_i\mathbf{a}_{i,j})\cdot \text{cof}(\mathbf{U}_i^2-\mathbf{I})\mathbf{n}_{i,j},\ B=\det(\mathbf{U}_i^2-\mathbf{I})-A/4, \tag{10}$$

where the symbol cof(·) means the cofactor of a matrix. The inequality (10) is algebraically equivalent to the criterion proposed in reference Ball and James (1987) to ensure the internally twinned martensite is compatible with austenite through a planar interface. Among all variants, pairs of variants $(\mathbf{U}_1,\mathbf{U}_2)$, $(\mathbf{U}_3,\mathbf{U}_4)$, $(\mathbf{U}_5,\mathbf{U}_6)$ form compound twins through one of the three cubic axes ⟨100⟩, however none of them are compatible with austenite, that means the inequality (10) is not satisfied. Examined by the criterion (10), the pairs of variants in the set

$$C=\{(p,3),(p,4),(p,5),(p,6),(q,5),(q,6) \text{ for } p=1,2,q=3,4\}$$

form compatible twin laminates for both type I and II twins through one of the face diagonal axes ⟨110⟩. That is $2|C|=24$ martensite twins. For each of the compatible twin laminates given by C, the crystallographic Eq. (9) gives 8 austenite/twinned martensite interfaces: 4 for type I twin and 4 for type II twin. In total, there are 96 austenite/twinned martensite interfaces under various twinning volume fractions, which can be expressed as a metric tensor

$$\mathbf{C}_{i,j}=(\mathbf{U}_i+f\mathbf{n}_{i,j}\otimes\mathbf{a}_{i,j})(\mathbf{U}_i+f\mathbf{a}_{i,j}\otimes\mathbf{n}_{i,j}) \tag{11}$$

for the twinned martensite variants $(i,j)\in C$ and $f\in[0,1]$.

The axial transformation strain for each of the twin systems along the loading direction $\hat{\mathbf{N}}=\mathbf{N}/|\mathbf{N}|$ is calculated as

$$\epsilon_{i,j}(\hat{\mathbf{N}})=\sqrt{\hat{\mathbf{N}}\cdot\mathbf{C}_{i,j}\hat{\mathbf{N}}}-1. \tag{12}$$

According to energy minimization (Bhattacharya et al., 2003; Bhattacharya and Kohn, 1996), the recoverable strain under uniaxial loading along $\hat{\mathbf{N}}$ can be found as

$$\epsilon_t(\hat{\mathbf{N}})=\max_{(i,j)\in C}\left(\epsilon_{i,j}(\hat{\mathbf{N}})\right). \tag{13}$$

Note that the metric tensor $\mathbf{C}_{i,j}$ for $(i,j)\in C$ always has a unity middle eigenvalue (Ball and James, 1987), then the crystallographic compatibility is guaranteed between austenite and twinned martensite variants (i,j) through a planar habit plane.

The calculated transformation strain under each of the loading directions is listed in Table 2, compared to the measured superelastic strain by microtension experiment, characterized as the plateau strain bounded between two linear elastic regimes of austenite and martensite as labeled in Fig. 6(a). Among all tested orientations, the predicted transformation strains of [223] and [1 2 14] oriented micro-slats agree with the characterized strains very well, while the theoretical strains are slightly smaller than the measured values for [325] and [205] orientations. It suggests that there exist a small amount of axial deformation not related to martensitic transformation in textures [325] and [205].

3.3. One-dimensional micromechanics constitutive model

In order to further understand the effect of crystallographic anisotropy on superelastic response, we consider a one-dimensional constitutive model for the micro-slat under uniaxial tension. The Helmholtz free energy density is written as a function of axial strain ϵ, internal variable λ and temperature θ,

$$\phi(\epsilon,\lambda,\theta=298\text{K})=\frac{1}{2}E_{\mathbf{N}}\left(\epsilon-\lambda\epsilon_t(\mathbf{N})\right)^2+\lambda\frac{\rho\ell}{\theta_c}(\theta-\theta_c)-c_p\theta\ln\left(\frac{\theta}{\theta_c}\right), \tag{14}$$

where θ_c is assumed to be the average transformation temperature, ℓ is the latent heat of phase transformation, and $\rho=7.3\text{g/cm}^3$ is the density of the material. The first term is bulk elastic energy density due to the tensile loading, where $E_{\mathbf{N}}$ is the elastic modulus along the tensile direction $\mathbf{N}$, corresponding to the relative axial elastic elongation along this direction. In this model, we assume that the energetic contribution due to the change in cross-sectional area is negligible within elastic and superelastic regimes. The second and third energetic terms underly the chemical energy density due to the thermally-driven phase transformation and the heat exchange with surroundings.

All thermal properties were characterized by DSC in Fig. 4(a). Since our experiment was performed under room temperature, the temperature θ in (14) is set to be 298 K. Upon loading, $\theta_c=\theta_c^{A\to M}=\frac{1}{2}(M_s+M_f)=235.5$ K, while upon unloading, $\theta_c=\theta_c^{M\to A}=\frac{1}{2}(A_s+A_f)=260.5$K. The directional elastic moduli of the testing orientations are calculated by cubic symmetry

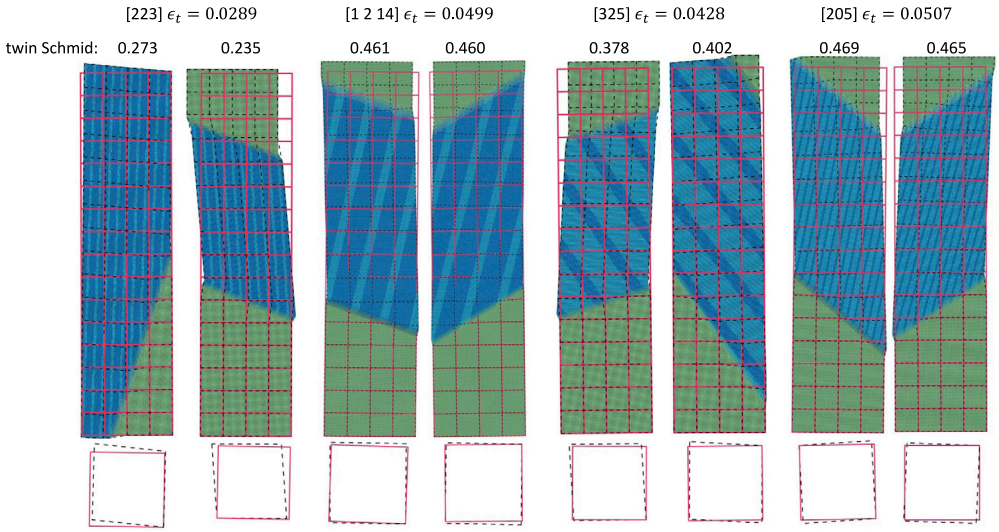

Fig. 7. Twin structures (blue and cyan stripes) formed in austenite (green) phase of (a)[223] (b) [1 2 14] (c) [325] (d) [205] oriented micro-slats during uniaxial tension in $Z - X$ plane. ϵ_t denote the axial tensile strain gained by phase transformation.

in (3): $E_{[205]} = 12.4$ GPa, $E_{[223]} = 50$ GPa, $E_{[325]} = 26$ GPa, $E_{[1\ 2\ 14]} = 8.6$ GPa. The internal variable $\lambda \in [0, 1]$ represents the volume fraction of martensite phase. The driving force with respect to the internal variable is defined as

$$d_\lambda = -\frac{\partial \phi}{\partial \lambda} = \epsilon_t(\mathbf{N}) E_{\mathbf{N}}(\epsilon - \lambda \epsilon_t(\mathbf{N})) - \frac{\rho \ell}{\theta_c}(\theta - \theta_c). \tag{15}$$

The constitutive relation of (14) gives the stress

$$\sigma = \frac{\partial \phi}{\partial \epsilon} = E_{\mathbf{N}}\left(\epsilon - \lambda \epsilon_t(\mathbf{N})\right). \tag{16}$$

Substitute (16) in (15), we obtain

$$d_\lambda = \sigma \epsilon_t(\mathbf{N}) - \frac{\rho \ell}{\theta_c}(\theta - \theta_c). \tag{17}$$

We assume that the evolution of martensite (*i.e.* evolution of λ) depends on the driving force d_λ through the kinetic relation (Sadjadpour and Bhattacharya, 2007)

$$\dot{\lambda} = \begin{cases} \left(1 + \frac{1}{d_\lambda - d^+}\right)^{-1/2} & d_\lambda > d^+, \\ \left(1 + \frac{1}{-d_\lambda + d^-}\right)^{-1/2} & d_\lambda < d^-, \\ 0 & \text{else.} \end{cases} \tag{18}$$

The parameters $d^\pm$ are the critical driving forces during loading and unloading paths. Based on (17), the critical driving force is given by $d^+ = -\rho \ell^{A \to M}(\theta - \theta_c)/\theta_c$ in absence of transformation strain, and $d^- = -d^+$. Under a linear loading profile

$$\sigma(t) = \begin{cases} \frac{2\sigma_{\max}}{\tau} t & t \le \tau/2, \\ \frac{-\sigma_{\max}}{\tau}(t - \tau/2) & t > \tau/2, \end{cases} \tag{19}$$

where the loading period $\tau = 45$sec, and maximum load $\sigma_{\max}$ is set to be 800 MPa for [223], 600 MPa for the other three orientations. The stress–strain behaviors are numerically calculated in Fig. 6(f), corresponding to the critical stress $\sigma_{cr} = 472.3$ MPa, 286.7 MPa, 337.9 MPa, and 282.4 MPa for [223], [1 2 14], [325] and [205] respectively. Our one-dimensional model agrees well with the stress-induced phase transformation for all textures captured by the microtension experiments. It confirms that the deformation mechanism at micron sizes is dominated by martensitic transformation. The critical transformation stress predicted by our one-dimensional constitutive model agrees very well with the experimental results for each of the textures. However, the orientation-dependent recoverable strains are relatively smaller than the measured values, especially for the orientation [205].

To explore the deformation mechanism that may cause the strain discrepancy between theory and experiment, we analyzed the twins and slips in details. The interfaces between austenite and twinned martensite are calculated and plotted in Fig. 7. For comparison, the slip planes of face-centered cubic (fcc) lattice with respect to the maximum slip Schmid factors are plotted in Fig. 8. By solving the crystallographic Eq. (9) and maximizing the uniaxial tensile strain in (13), for the [223] and [1 2 14] oriented micro-slats, the martensite is twinned through $(1\bar{1}0)$ type I twin by variants $(1, 4)$ with the volume fraction $f = 0.713$; for the [205]

Table 3
The habit plane, lateral shear strain ($Z-X$ shear) and corresponding maximum Schmid factors of twinned martensite in [223], [1 2 14], [325] and [205] oriented micro-slats.

N	variants	habit plane	shear strain ϵ_{31}	twin Schmid	slip Schmid
[223]	(1, 4)	(−0.659, 0.256, 0.707)	0.0783	0.273	0.356
[1 2 14]		(−0.753, −0.179, −0.633)	0.0124	0.461	0.463
[325]	(1, 4)	(−0.256, 0.659, −0.707)	0.0490	0.402	0.456
[205]		(0.179, 0.753, 0.633)	0.0105	0.469	0.497

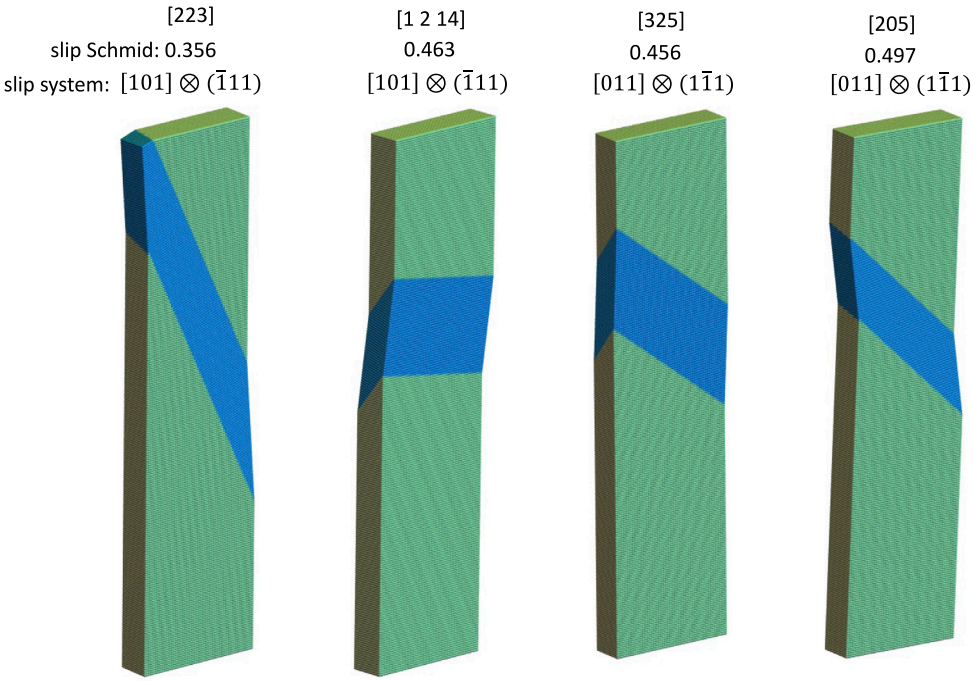

Fig. 8. Slip structures (blue) in austenite (green) phase of (a)[223] (b) [1 2 14] (c) [325] (d) [205] oriented micro-slats during uniaxial tension in $Z-X$ plane.

and [325] oriented micro-slats, the martensite is also twinned through the same pair of variants yet with a different volume fraction $f = 0.287$. Along the loading direction $\mathbf{Z}$ listed in Table 1, The twin Schmid factor is calculated as $m_t(\mathbf{Z}) = (\mathbf{Z}\cdot\mathbf{m})(\mathbf{Z}\cdot\mathbf{b})/(|\mathbf{Z}|^2|\mathbf{m}||\mathbf{b}|)$ for specific habit plane $\mathbf{m}$ and shear vector $\mathbf{b}$ as the solution to Eq. (9). Note that the crystallographic orientations are denoted by $\mathbf{N}$ = [223], [1 2 14], [325] and [205], numerically we use the exact components of the Z axis listed in Table 1. The calculated austenite/twinned martensite habit planes are listed in Table 3, corresponding to the microstructure for twinned martensite laminates (blue) and undeformed austenite (green) shown in Fig. 7. We also present the deformed configuration (black dashed frame) by the homogeneous deformation gradient $\mathbf{I}+\mathbf{b}\otimes\mathbf{m}$, compared to the reference configuration depicted as the red square in Fig. 7. From kinematics point of view, the shear deformation of [205] is the least among all textures.

A quantitative comparison of the lateral shear deformation can be conducted by a direct calculation of $Z-X$ shear component. For variant pairs $(1,4)$ and some twinning volume fraction f such that the metric tensor $\mathbf{C}_{1,4}(f)$ is compatible with the austenite, the shear component

$$\epsilon_{31}(\mathbf{X},\mathbf{Z}) = \frac{\mathbf{X}\cdot\mathbf{C}_{1,4}(f)\mathbf{Z}}{(\mathbf{X}\cdot\mathbf{C}_{1,4}(f)\mathbf{X})^{1/2}(\mathbf{Z}\cdot\mathbf{C}_{1,4}(f)\mathbf{Z})^{1/2}}, \tag{20}$$

where $\mathbf{X}$ and $\mathbf{Z}$ are the axes of the tested microslat listed in Table 1, and the metric tensor $\mathbf{C}_{1,4}(f) = (\mathbf{U}_1+f\mathbf{n}_{1,4}\otimes\mathbf{a}_{1,4})(\mathbf{U}_1+f\mathbf{a}_{1,4}\otimes\mathbf{n}_{1,4})$ for volume fraction $f = 0.713$ for [223] and [1 2 14] orientations and $f = 0.287$ for [325] and [205]. The results of $Z-X$ shear strains are given in the third column of Table 3, among which the shear deformation of [205] oriented micro-slat is the smallest. In contrast, its twin Schmid factor and fcc slip Schmid factor is the highest compared to other three orientations. Note that [205] is also the orientation showing the largest elongation. It strongly suggests that the high tendency of plastic flow along both habit planes and slip planes may activate the motion of defects, which accumulate at the surface. Due to massive normal stretching, the accumulated defects form nano-cavities at the side surface, as seen in the deformed configuration of [205] micro-slat in Fig. 6(e). The stress-induced martensitic transformation, together with the elastic stretching of cavities make the characterized recoverable strain of [205] bigger than the theoretically predicted transformation strain.

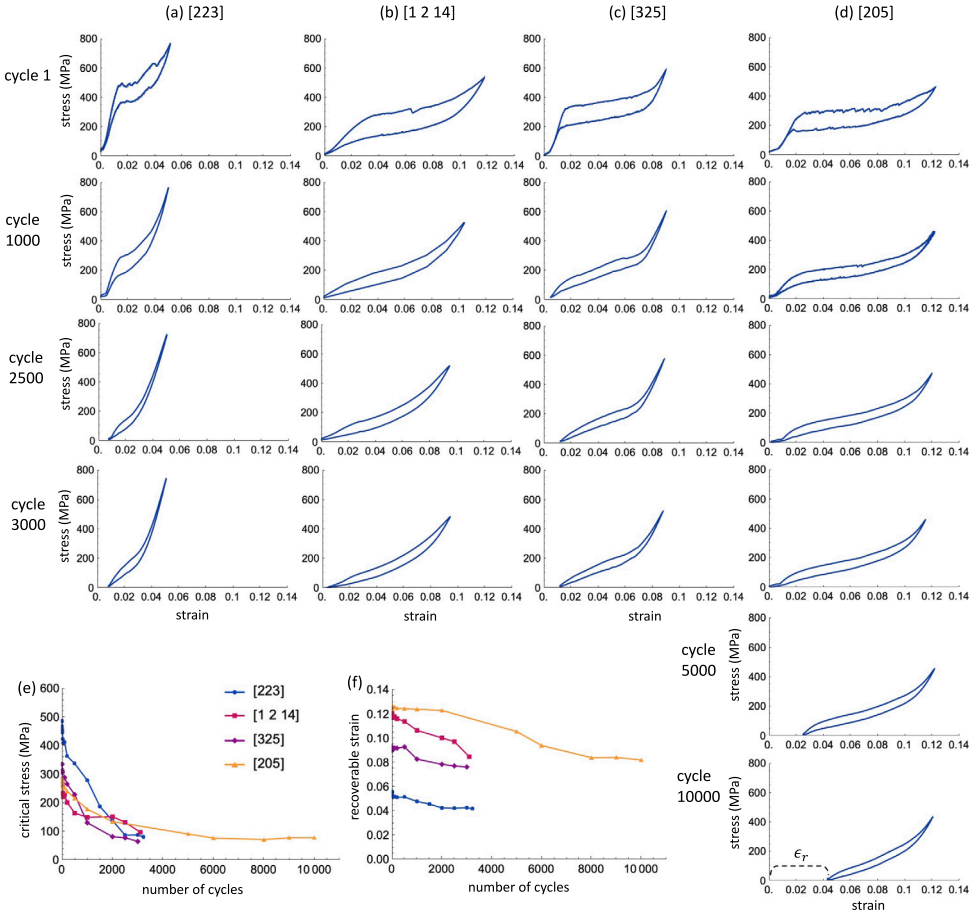

Fig. 9. Tensile cyclic nanomechanical behaviors of the $Cu_{67}Al_{24}Mn_9$ micro-slats oriented in (a) [223], (b) [1 2 14], (c) [205], and (d) [325] with the functional degradation of (e) critical stress and (f) recoverable strain.

3.4. Tensile functional fatigue under cyclic stress-induced transformations at micron-scale

To study the degradation of superelasticity and structural fracture mechanism, we conducted an in situ microtension fatigue test for each of the micro-slats in various orientations. Fig. 9a–d illustrates the stress–strain responses of the [223], [1 2 14], [325] and [205] oriented micro-slats at various number of cycles. The superelastic behavior is captured in all orientations before fracture, although their functionalities gradually degrade as increasing the number of cycles. The cyclic degradation of critical stress and recoverable strain is shown in Fig. 9(e) and (f). The [223], [1 2 14] and [325] oriented micro-slats fracture under 3000 cycles of stress-induced phase transformations, while the [205] oriented micro-slat is still functional even after 10,000 cycles without failure. For the [205] oriented micro-slat, the critical stress and the total recoverable strain are asymptotically converged after 6,000 transformation cycles. Interestingly, the recoverable strain remains above 8% despite an accumulation of large permanent strain (*i.e.* ϵ_r labeled in Fig. 9d).

From the surface morphology captured by SEM after a specific number of fatigue cycle (Fig. 10), it is clearly seen that the nano-cavities grow along the tensile direction in [205] oriented micro-slat but no structural fracture occurs, while the cracks form and propagate in [223], [1 2 14] and [325] micro-slats. The fracture mechanisms are different in different crystallographic textures. For textures [223], [1 2 14] and [325], the structure failure is caused by shear, Fig. 10(a)–(c). Both critical stress and recoverable strain gradually decrease upon repeated phase transformations, shown in Fig. 9(e)–(f). Among them, the most stiff texture [223] degrades the fastest, which almost loses the superelastic feature after 2500 cycles. For [325] texture, the crack appears within the swelling region of the micro-slat. The crack nucleation may be sensitive to intrinsic defect distributions inside the sample. We fabricated two tensile slat of [325] texture within the same grain, and we got similar mechanical life and cracking mode. For [205] texture, the structural and functional fatigue mechanism is a combination of plasticity and stretchability of nano-cavities. Because both twinning and slip Schmid factors are large, the plastic flow drives the defects to the side and form nano-cavities. When martensitic transformation takes place, stress-induced massive stretching make the cavity elongate along the tensile direction in addition to the axial transformation strain. Upon unloading, the cavity partially recovered. This process repeats over numerous transformation cycles, as a result the residual strain caused by formation of cavity accumulates but the main body's superelasticity does not degrade

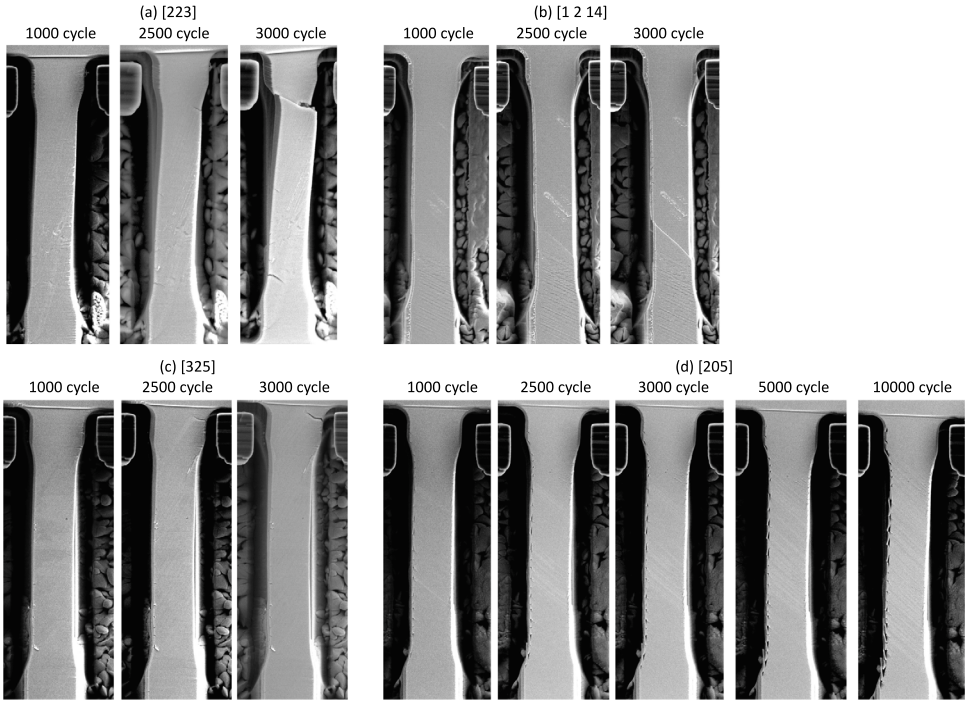

Fig. 10. Surface morphology of the $Cu_{67}Al_{24}Mn_9$ micro-slats oriented in (a) [223], (b) [1 2 14], (c) [205], and (*d*)[325] at various cycles during the in situ microtension fatigue tests.

Table 4
Orientation-dependent yield strength of $Cu_{67}Al_{24}Mn_9$ with the critical resolved shear stress $\tau_{CRSS} = 401.6$ MPa.

Orientation	Yield strength σ_y	Yielding mode	σ_{cr}/σ_y
[223]	1128 MPa	$[101] \otimes (\bar{1}11)$ slip	0.42
[1 2 14]	867 MPa	$[101] \otimes (\bar{1}11)$ slip	0.33
[325]	881 MPa	$[011] \otimes (1\bar{1}1)$ slip	0.38
[205]	818 MPa	$[011] \otimes (1\bar{1}1)$ slip	0.35

too much. Although similar stress–strain response is captured in [1 2 14] texture (Fig. 9b), its lateral shear deformation is relatively larger than that of [205] texture. From its microstructure, we did not observe formation of cavities at visible length scales under SEM. Therefore, we conjecture that the deformation mechanism of [1 2 14] texture is different from [205] texture.

From microscopic point of view, both dislocation motions and formation of twins may cause the permanent strain during the uniaxial tensile loading. The activation of dislocation follows the Schmid law. When the resolved shear stress on the slip plane reaches τ_{CRSS}, the dislocations slip, and the permanent strain is accumulated. The axial stress $\sigma_s(\mathbf{t}) = \frac{\tau_{CRSS}}{m^*(\mathbf{t})}$ is defined as the yield strength due to dislocation motions where m^* is the maximum Schmid factor of fcc slip system along the tensile direction $\mathbf{t}$. On the other hand, the formation of deformation twins also causes the permanent strain by the shear motion with respect to austenite. When the resolved shear stress on the A/M interface reaches τ_{CRSS}, the axial stress $\sigma_{tw}(\mathbf{t}) = \frac{\tau_{CRSS}}{m_t(\mathbf{t})}$ is defined as the yielding strength due to twinning where m_t is the maximum twinning Schmid factor along the tensile direction $\mathbf{t}$. For a micro-slat undergoing stress-induced martensitic transformation, the sample yields when the axial stress reaches the least value of $\{\sigma_s, \sigma_{tw}\}$, thus we can estimate the orientation-dependent yield strength as

$$\sigma_y(\mathbf{t}) = \min\left\{\sigma_{tw}(\mathbf{t}), \sigma_s(\mathbf{t})\right\}. \tag{21}$$

Table 4 concludes the calculated yield strength for each of the tested orientations corresponding to the specific yielding mode. The results suggest that the martensitic transformation occur prior to the plastic deformation since the critical transformation stress is less than the yield strength for all of them. As expected, the texture [205] has the lowest yield strength. We calculated the ratio of transformation stress (σ_{cr}) to the yield strength (σ_y) in the last column of Table 4, which can be used as an index to check the tendency of martensitic transformation and plastic deformation upon loading. Even the stress flow inside the tensile sample is below the yield limit, the plastic deformation still possibly occur for those orientation with relatively high transformation stress, such as the texture [223]. Experimentally, this texture indeed degrades the fastest within first 1000 stress-induced transformation cycles (Fig. 9e–f).

4. Conclusion

In this paper, we carried out a comprehensive experimental and theoretical study of orientation-dependent superelastic behaviors of $Cu_{67}Al_{24}Mn_9$ alloy at small scales by in situ micromechanical tensile experiment under scanning electron microscopy. We showed that the stress-induced martensitic transformation and corresponding fatigue resistance are much texture dependent. Our one-dimensional constitutive model well captured the main crystallographic anisotropy of the stress-induced martensitic transformation, which also suggests some latent mechanism for specific texture, e.g. [205]. Through in situ observation of microstructure at the maximum stretched configuration, we discovered formation of nano-cavities in [205] texture. By geometric nonlinear analysis of martensite microstructure and fcc slip systems, we conclude that the massive normal elongation, suppressed lateral shear and high tendency of plastic flow cause the formation, stretching and growth of nano-cavities at one side of the tensile slat at micron scales.

Declaration of competing interest

The authors declare that they have no known competing financial interests or personal relationships that could have appeared to influence the work reported in this paper.

Acknowledgments

M. K. and X. C. thank the financial support under GRF Grants 16201118 and 16201019 by Research Grants Council, Hong Kong. M. K., X. C. K. C. and Q. S. thank the financial support CRF Grant No. C6016-20G-C also by Research Grants Council, Hong Kong. Q. S. thanks the Project of Hetao Shenzhen-Hong Kong Science and Technology Innovation Cooperation Zone (HZQB-KCZYB-2020083), the Science, Technology and Innovation Commission of Shenzhen Municipality of China (Project No. SGDX2019081623360564).

References

Ball, J., James, R., 1987. Fine phase mixtures as minimizers of energy. Arch. Ration. Mech. Anal. 100, 15–52.
Bhattacharya, K., Kohn, R.V., 1996. Symmetry, texture and the recoverable strain of shape-memory polycrystals. Acta Mater. 44, 529–542.
Bhattacharya, K., et al., 2003. Microstructure Of Martensite: Why It Forms And How It Gives Rise to The Shape-Memory Effect, Vol. 2. Oxford University Press.
Chen, Y., Howe, C., Lee, Y., Cheon, S., Yeo, W.-H., Chun, Y., 2016. Microstructured thin film nitinol for a neurovascular flow-diverter. Sci. Rep. 6 (1), 1–10.
Chen, M., Yang, X., Hu, R., Cui, Z., Man, H., 2004. Bioactive NiTi shape memory alloy used as bone bonding implants. Mater. Sci. Eng. C 24 (4), 497–502.
Chu, K., Yan, K., Ren, F., Sun, Q., 2019. A dual-pillar method for measurement of stress-strain response of material at microscale. Scr. Mater. 172, 138–143.
Dang, C., Chou, J.-P., Dai, B., Chou, C.-T., Yang, Y., Fan, R., Lin, W., Meng, F., Hu, A., Zhu, J., et al., 2021. Achieving large uniform tensile elasticity in microfabricated diamond. Science 371, 76–78.
Fornell, J., Tuncer, N., Schuh, C., 2017. Orientation dependence in superelastic Cu-Al-Mn-Ni micropillars. J. Alloys Compd. 693, 1205–1213.
Frick, C.P., Clark, B.G., Orso, S., Sonnweber-Ribic, P., Arzt, E., 2008. Orientation-independent pseudoelasticity in small-scale NiTi compression pillars. Scr. Mater. 59, 7–10.
Frick, C., Orso, S., Arzt, E., 2007. Loss of pseudoelasticity in nickel–titanium sub-micron compression pillars. Acta Mater. 55, 3845–3855.
Gao, H., Huang, Y., Nix, W., Hutchinson, J., 1999. Mechanism-based strain gradient plasticity—I. Theory. J. Mech. Phys. Solids 47 (6), 1239–1263.
Gómez-Cortés, J.F., Nó, M.L., López-Ferreño, I., Hernández-Saz, J., Molina, S.I., Chuvilin, A., San Juan, J.M., 2017. Size effect and scaling power-law for superelasticity in shape-memory alloys at the nanoscale. Nature Nanotechnol. 12 (8), 790.
Gómez-Cortés, J.F., Nó, M.L., Ruíz-Larrea, I., Breczewski, T., López-Echarrí, A., Schuh, C.A., San Juan, J.M., 2019. Ultrahigh superelastic damping at the nano-scale: A robust phenomenon to improve smart MEMS devices. Acta Mater. 166, 346–356.
Greer, J.R., Nix, W.D., 2006. Nanoscale gold pillars strengthened through dislocation starvation. Phys. Rev. B 73 (24), 245410.
Greer, J.R., Oliver, W.C., Nix, W.D., 2005. Size dependence of mechanical properties of gold at the micron scale in the absence of strain gradients. Acta Mater. 53, 1821–1830.
Hua, P., Chu, K., Ren, F., Sun, Q., 2020. Cyclic phase transformation behavior of nanocrystalline NiTi at microscale. Acta Mater. 185, 507–517.
Hua, P., Chu, K., Sun, Q., 2018. Grain refinement and amorphization in nanocrystalline NiTi micropillars under uniaxial compression. Scr. Mater. 154, 123–126.
Huang, Y., Gao, H., Nix, W., Hutchinson, J., 2000. Mechanism-based strain gradient plasticity—II. Analysis. J. Mech. Phys. Solids 48 (1), 99–128.
Jennings, A.T., Greer, J.R., 2011. Tensile deformation of electroplated copper nanopillars. Phil. Mag. 91, 1108–1120.
Kabirifar, P., Chu, K., Ren, F., Sun, Q., 2018. Effects of grain size on compressive behavior of NiTi polycrystalline superelastic macro-and micropillars. Mater. Lett. 214, 53–55.
Karami, M., Chen, X., 2021. Nanomechanics of shape memory alloys. Mater. Today Adv. 10, 100141.
Karami, M., Tamura, N., Yang, Y., Chen, X., 2020a. Derived crystal structure of martensitic materials by solid–solid phase transformation. Acta Crystallogr. Sect. A Found. Adv. 76, 521–533.
Karami, M., Zhu, Z., Zeng, Z., Tamura, N., Yang, Y., Chen, X., 2020b. Two-tier compatibility of superelastic bicrystal micropillar at grain boundary. Nano Lett. 20, 8332–8338.
Kiener, D., Grosinger, W., Dehm, G., Pippan, R., 2008. A further step towards an understanding of size-dependent crystal plasticity: In situ tension experiments of miniaturized single-crystal copper samples. Acta Mater. 56 (3), 580–592.
Kiener, D., Minor, A.M., 2011. Source truncation and exhaustion: insights from quantitative in situ TEM tensile testing. Nano Lett. 11 (9), 3816–3820.
Kim, J.-Y., Greer, J.R., 2009. Tensile and compressive behavior of gold and molybdenum single crystals at the nano-scale. Acta Mater. 57 (17), 5245–5253.
Kim, J.-Y., Jang, D., Greer, J.R., 2010. Tensile and compressive behavior of tungsten, molybdenum, tantalum and niobium at the nanoscale. Acta Mater. 58, 2355–2363.
Kim, J.-Y., Jang, D., Greer, J.R., 2012. Crystallographic orientation and size dependence of tension–compression asymmetry in molybdenum nano-pillars. Int. J. Plast. 28, 46–52.
Koledov, V., von Gratowski, S., Nguyen, H.D., Thi, H.L.N., Vu, H.K., Santos, G.N., Oo, T.Z., 2019. Nano-manipulation and nano-assembling using shape memory alloy nanogripper of metal oxide and semiconductor single nanowires and nanoparticles for biological nanosensors. Adv. Nat. Sci. Nanosci. Nanotechnol. 10 (3), 035003.
Morgan, N., 2004. Medical shape memory alloy applications—the market and its products. Mater. Sci. Eng. A 378 (1–2), 16–23.

Ni, X., Greer, J.R., Bhattacharya, K., James, R.D., Chen, X., 2016. Exceptional resilience of small-scale $Au_{30}Cu_{25}Zn_{45}$ under cyclic stress-induced phase transformation. Nano Lett. 16, 7621–7625.

Nix, W.D., Gao, H., 1998. Indentation size effects in crystalline materials: a law for strain gradient plasticity. J. Mech. Phys. Solids 46 (3), 411–425.

Norfleet, D., Sarosi, P., Manchiraju, S., Wagner, M.-X., Uchic, M., Anderson, P., Mills, M., 2009. Transformation-induced plasticity during pseudoelastic deformation in Ni–Ti microcrystals. Acta Mater. 57, 3549–3561.

Oh, S.H., Legros, M., Kiener, D., Dehm, G., 2009. In situ observation of dislocation nucleation and escape in a submicrometre aluminium single crystal. Nature Mater. 8, 95–100.

Petrini, L., Migliavacca, F., 2011. Biomedical applications of shape memory alloys. J. Metall. 2011.

Pfetzing-Micklich, J., Ghisleni, R., Simon, T., Somsen, C., Michler, J., Eggeler, G., 2012. Orientation dependence of stress-induced phase transformation and dislocation plasticity in NiTi shape memory alloys on the micro scale. Mater. Sci. Eng. A 538, 265–271.

Sadjadpour, A., Bhattacharya, K., 2007. A micromechanics inspired constitutive model for shape-memory alloys: the one-dimensional case. Smart Mater. Struct. 16 (1), S51.

San Juan, J., Nó, M.L., Schuh, C.A., 2008. Superelasticity and shape memory in micro-and nanometer-scale pillars. Adv. Mater. 20 (2), 272–278.

San Juan, J., Nó, M.L., Schuh, C.A., 2009. Nanoscale shape-memory alloys for ultrahigh mechanical damping. Nature Nanotechnol. 4 (7), 415–419.

San Juan, J., Nó, M., Schuh, C., 2012. Superelastic cycling of Cu–Al–Ni shape memory alloy micropillars. Acta Mater. 60, 4093–4106.

Sehitoglu, H., Anderson, R., Karaman, I., Gall, K., Chumlyakov, Y., 2001. Cyclic deformation behavior of single crystal NiTi. Mater. Sci. Eng. A 314 (1–2), 67–74.

Tian, L., Cheng, Y.-Q., Shan, Z.-W., Li, J., Wang, C.-C., Han, X.-D., Sun, J., Ma, E., 2012. Approaching the ideal elastic limit of metallic glasses. Nature Commun. 3, 1–6.

Wei, Y., Hutchinson, J.W., 2003. Hardness trends in micron scale indentation. J. Mech. Phys. Solids 51 (11–12), 2037–2056.

Yoneyama, T., Miyazaki, S., 2008. Shape Memory Alloys For Biomedical Applications. CRC Press, Boca Raton, FL.